Imaging Shapes of Atomic Nuclei in High-Energy Nuclear Collisions

STAR Collaboration

Atomic nuclei are self-organized, many-body quantum systems bound by strong nuclear forces within femtometer-scale space. These complex systems manifest a diverse set of shapes [1, 2], traditionally explored via non-invasive spectroscopic techniques at low energies [3, 4]. Their instantaneous shapes, obscured by long-timescale quantum fluctuations, are considered not directly observable at low energy. We introduce a complementary method, collective flow assisted nuclear shape imaging, to image the nuclear global shape by colliding them at ultrarelativistic speeds and analyzing the collective response of outgoing debris. This technique captures a collision-specific snapshot of the spatial matter distribution in the nuclei, which, through the hydrodynamic expansion, leaves imprints on the particle momentum distribution patterns observed in detectors [5, 6]. We benchmark this method in collisions of ground state Uranium-238 nuclei, known for its elongated, axial-symmetric shape. Our findings, while confirming an overall deformation broadly consistent with prior low-energy experiments, also indicate a small deviation from axial symmetry in the nuclear ground state. This approach marks a new way of imaging nuclei, especially those with uncertain shape characteristics, and refines initial conditions in high-energy nuclear collisions. It tackles the important issue of nuclear structure evolution across various energy scales.

More than 99.9% of the visible matter in the cosmos resides in the center of atoms – the atomic nuclei composed of nucleons (protons and neutrons). Our present knowledge of their global structure primarily comes from a variety of spectroscopic or scattering experiments [3, 4, 7] at beam energies below hundreds of MeV per nucleon. These studies reveal that most nuclei are ellipsoidally deformed, with greater deformation in nuclei distant from magic numbers (2, 8, 20, 28, 50, 82, and 126) [8]. Investigating this deformation across the nuclear chart has been an important area of research over many decades, and is crucial for topics such as nucleosynthesis [9], nuclear fission [10], and neutrinoless double beta decay ($0\nu\beta\beta$) [11].

Within a collective model picture, the ellipsoidal shape of a nucleus with mass number A is defined in the intrinsic (body-fixed) frame, where its surface $R(\theta, \phi)$ is described by [1],

$$R(\theta,\phi) = R_0\big(1 + \beta_2[\cos\gamma Y_{2,0} + \sin\gamma Y_{2,2}]\big) . \quad (1)$$

Here, $R_0 \approx 1.2A^{1/3}$ fm represents the nuclear radius (about 5–8 fm for large nuclei). The spherical harmonics in the real basis $Y_{l,m}(\theta,\phi)$, the quadrupole deformation magnitude β_2, and the triaxiality parameter γ define the nuclear shape. The γ parameter, spanning 0° to 60°, controls the ratios of principal radii. Specifically, $\gamma = 0°$ corresponds to a prolate shape, $\gamma = 60°$ an oblate shape, and values in between $0° < \gamma < 60°$ to a triaxial shape. While most nuclei are axially-symmetric (prolate or oblate) or have a fluctuating γ value (γ-soft), rigid triaxial shape is uncommon [12]. An example of an axial-symmetric, prolate-deformed nucleus is shown in Fig. 1a.

Nuclear shapes, even in ground states, are not fixed. They exhibit zero-point quantum fluctuations involving various collective and nucleonic degrees of freedom (DOF) at different timescales. These fluctuations superimpose on each other in the laboratory frame. In well-

deformed nuclei like ^{238}U, dominant fluctuations are in the rotational DOF with a timescale of $\tau_{\rm rot} \sim I/\hbar \sim 10^3$–$10^4$ fm/c (1 fm/c = 3×10^{-24} seconds) [13], where I denotes the moment of inertia (Fig. 1b). Consequently, measurement processes in spectroscopic methods, lasting orders of magnitude longer than $\tau_{\rm rot}$, capture a coherent superposition of wavefunctions in all orientations, obscuring instantaneous nuclear shapes. However, these shapes can be extracted precisely by comparing spectroscopic data (Fig. 1c) with model calculations [14, 15]. Traditional electron-nucleus scattering experiments, though faster than $\tau_{\rm rot}$, probe mostly localized regions of the nucleus, resulting in an orientation-averaged spherical image after accumulating many events, where the impact of nuclear deformation manifests as a broadening of the charge distribution [1, 7].

New shape-imaging method. To directly observe the nuclei's global shape, a measurement must 1) be much quicker than $\tau_{\rm rot}$ and 2) provide access to the many-body nucleon distribution in each nucleus, which contains the frame-independent shape information. High-energy nuclear collisions, an utterly destructive process, remarkably fulfill these criteria. Conducted at the Relativistic Heavy-Ion Collider (RHIC) and the Large Hadron Collider (LHC) with center-of-mass energies per nucleon pair ($\sqrt{s_{\rm NN}}$) reaching up to 5000 GeV, these collisions completely obliterate the nuclei, temporarily forming a quark-gluon plasma (QGP) – a hot, dense matter of interacting quarks and gluons [5, 6, 16, 17]. The nuclear shape influences the QGP's geometry and its collective expansion, imprinting itself on the momentum distribution of the produced particles. In an ironic twist, this effectively realizes Richard Feynman's analogy of the seemingly impossible task of "figuring out a pocket watch by smashing two together and observing the flying debris," and the collective response plays a key role.
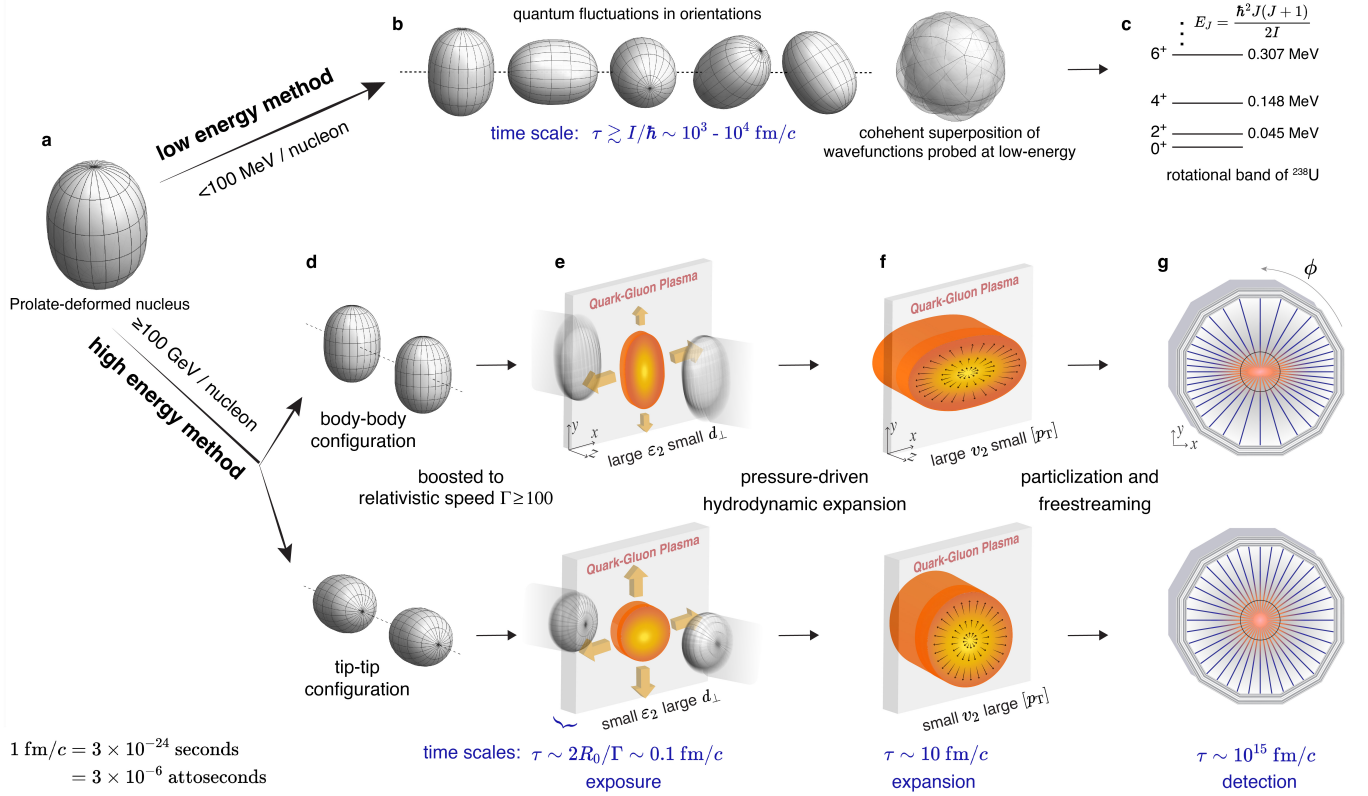
Fig. 1 | Methods for determining the nuclear shape in low and high energies. **a,** cartoon of a well-deformed prolate-shaped nucleus. **b,** quantum fluctuations over Euler angles for this nucleus and associated overall timescale. **c,** quantum mechanical manifestation of the deformation in terms of the first rotational band of ^{238}U. **d,** aligning the two nuclei in headon body-body configuration (top) and tip-tip configuration (bottom). **e,** collision of two Lorentz-contracted nuclei at high energy and resulting 3D profile of the initially-produced quark-gluon plasma, where arrows indicate the pressure gradients. **f,** 3D profile of the quark-gluon plasma at the end of the hydrodynamic expansion before freezes out into particles, where arrows indicate the velocities of fluid cells. **g,** charged particle tracks measured in the detector. The timescales shown are in units of fm/c – the time for light to travel one femtometer. The body-body configuration has large eccentricity ε_2 and small gradient $d_\perp$, leading to large elliptic flow v_2 and smaller average transverse momentum $[p_{\rm T}]$, and verse versa for tip-tip configuration (see text).

Our shape-imaging technique focuses on headon (near zero impact parameter) collisions of prolate-deformed nuclei (Fig. 1d-g). The initial configurations lie between two extremes: body-body (top) and tip-tip (bottom) collisions (Fig. 1d). Prior to impact, Lorentz-contraction flattens the ground state nuclei into pancake-like shapes by a factor of $\Gamma = \frac{1}{2}\sqrt{s_{\rm NN}}/m_0 > 100$, where $m_0 \approx 0.94$ GeV is the nucleon mass (Fig. 1e). The initial impact, lasting $\tau_{\rm expo} = 2R_0/\Gamma \lesssim 0.1$ fm/c, acts as an exposure time. The shape and size of the overlap region, reflecting the initially-produced QGP, directly mirror those of the colliding nuclei projected on the transverse (xy) plane (Fig. 1e). Body-body collisions create a larger, elongated QGP, which undergoes pressure-gradient-driven expansion (indicated by arrows) until about 10 fm/c [6], resulting in an inverted, asymmetric distribution (Fig. 1f). In contrast, tip-tip collisions form a compact, circular QGP, driving a more rapid but near symmetric expansion (Fig. 1f). In the final stage, the QGP freezes out

into thousands of particles, captured as tracks in detectors, whose angular distributions reflect the initial QGP shape (Fig. 1g). This flow-assisted imaging is akin to the Coulomb Explosion Imaging in molecule structure analysis [18–22], where the spatial arrangement of atoms, ionized by an X-ray laser or through passage in thin foils, is deduced from their mutual Coulomb-repulsion-driven expansion. However, the expansion duration in high-energy collisions is about 10^6–10^9 times shorter.

Energy evolution of shapes? A pertinent question arises: How do the nuclear shapes observed in high-energy colliders compare to those derived from low-energy experiments? For well-deformed nuclei like ^{238}U, we expect them to align at a basic level. However, there are other correlations (collective vibration, clustering, short-range correlations, etc.) that manifest over increasingly faster timescales from 1000 to a few fm/c [23]. Moreover, high-energy collisions also probe nuclear structure at subnucleonic level, such as quark and gluon

correlations, and modifications caused by dense gluon fields [24]. As a result, the deformations observed at high energy might differ from those at low energy. These factors are subdominant for well-deformed nuclei but could be more discernible for less-deformed ones. This highlights the need to examine nuclear phenomena across energy scales and discover new phenomena.

Observables. In Fig. 1e, the QGP's initial shape is quantified by the eccentricity, $\varepsilon_2 = \frac{\langle y^2 \rangle - \langle x^2 \rangle}{\langle y^2 \rangle + \langle x^2 \rangle}$, calculated from the nucleon distribution in the xy-plane, perpendicular to the beam direction. The hydrodynamic expansion, reacting to ε_2, results in particle anisotropy, described as $dN/d\phi \propto 1 + 2v_2 \cos(2\phi)$ aligned with the impact parameter along the x-axis. This phenomenon, known as "elliptic flow" (v_2) [25], is depicted in Fig. 1g. Additionally, the QGP's compactness or density gradient, indicated by the overlap's inverse area $d_\perp = 1/\sqrt{\langle x^2 \rangle \langle y^2 \rangle}$ [26], influences the radial expansion or "radial flow", captured in the event-wise average transverse momentum ($[p_T]$). A key discovery at RHIC was the QGP's behavior as a nearly perfect, inviscid fluid [27, 28], effectively transforming initial geometry into final state anisotropies. Hydrodynamic models have confirmed linear response relations: $v_2 \propto \varepsilon_2$ [29] and $\delta p_T \propto \delta d_\perp$ [30], where $\delta p_T = [p_T] - \langle [p_T] \rangle$ and $\delta d_\perp = d_\perp - \langle d_\perp \rangle$ denote event-wise deviations from mean values.

In collisions with spherical nuclei, non-zero ε_2 and $\delta d_\perp$ can be generated by the random fluctuations in the position of nucleons in the overlap region. In non-headon collisions, besides these stochastic elements, the overlap region also has an average elliptical shape. This average shape significantly contributes to ε_2, known as reaction plane eccentricity $\varepsilon_2^{\rm rp}$ [31], but has little effect on $\delta d_\perp$.

Prolate deformation in the colliding nuclei further modifies ε_2 and $d_\perp$. Body-body collisions in this context yield high ε_2 and low $d_\perp$ values, and vice versa for tip-tip collisions. This leads to enhanced, anti-correlated event-by-event fluctuations in ε_2 and $d_\perp$ [32], measurable through observables like $\langle v_2^2 \rangle$, $\langle (\delta p_T)^2 \rangle$, and $\langle v_2^2 \delta p_T \rangle$ that are linearly related to the moments of the initial condition $\langle \varepsilon_2^2 \rangle$, $\langle (\delta d_\perp)^2 \rangle$, and $\langle \varepsilon_2^2 \delta d_\perp \rangle$. These observables, linked to two- and three-body nucleon distributions in the intrinsic frame (Methods), were found to have a simple parametric dependence on the nuclear shape [33]:

$$\langle v_2^2 \rangle = a_1 + b_1 \beta_2^2 \,,$$
$$\langle (\delta p_T)^2 \rangle = a_2 + b_2 \beta_2^2 \,,$$
$$\langle v_2^2 \delta p_T \rangle = a_3 - b_3 \beta_2^3 \cos(3\gamma) \,. \tag{2}$$

The positive coefficients a_n and b_n reflect the collision geometry and QGP properties. The b_n values are nearly independent of the impact parameter, while a_n values are minimized in headon collisions, making such collisions ideal for constraining nuclear shape. Our study represents the first quantitative, simultaneous determination of β_2 and γ using all three observables in Eq. (2).

Experimental setup. We conduct measurements with ^{238}U+^{238}U and ^{197}Au+^{197}Au collisions at $\sqrt{s_{\rm NN}}$ = 193 GeV and 200 GeV, respectively, using the STAR detector at RHIC. These species have contrasting shapes: mildly oblate ^{197}Au (close to magic numbers with Z=79 protons and N=118 neutrons) and highly prolate ^{238}U (an open shell nucleus with 92 protons and 146 neutrons). This comparison helps us to deduce ^{238}U's shape. A state-of-the-art beyond mean-field model prediction for ^{197}Au's deformation ranges in $\beta_{2\rm Au} \approx 0.12$–0.14 [34]. The ^{238}U's deformation, usually inferred from model fits to rotational spectra [35–38], is estimated at $\beta_{2\rm U} = 0.287 \pm 0.009$, which describes the shape for the mass distribution. Converting to a surface deformation via a liquid drop model usually leads to a slightly smaller $\beta_{2\rm U}$ value [39].

Rigorous calculations of the triaxiality for prolate-like heavy nuclei were limited [40, 41], with early estimates typically based on simple geometric rotor models, suggesting $\gamma_{\rm U} = 6°$–8° [42]. A sophisticated energy density functional calculation based on a collective Hamiltonian method (Gogny-5DCH) predicts $\gamma_{\rm U} \sim 8°$ [36]. A more recent analysis via a microscopic model suggests a rigid triaxiality with $\gamma_{\rm U} \sim 15°$ [43]. However, the origin of triaxiality in these nuclei (rotational or vibrational) remains debated [44]. Recent advances in the Monte-Carlo Shell Model enabled a more quantitative analysis, indicating a minor rigid triaxial component leading to a small non-zero γ for these nuclei, in alignment with spectra data [45]. However, triaxiality may change when nuclei are excited, complicating direct spectroscopic verification [45]. Thus, measuring ^{238}U's shape could validate our imaging method and directly investigate its ground-state triaxiality.

Our analysis uses U+U data from 2012 and Au+Au data from 2010 and 2011. Each collision produces up to 2000 charged particles in the STAR time-projection chamber (TPC) [46], covering the polar angle range $|\theta - 90°| \lesssim 50°$ and full ϕ range. The TPC tracks these particles and determines their p_T. Collision events are categorized by "centrality", defined as the percentage of the total inelastic cross-section, with lower percentages indicating more headon collisions. We calculate $\langle v_2^2 \rangle$, $\langle (\delta p_T)^2 \rangle$, and $\langle v_2^2 \delta p_T \rangle$ via established methods [47] using tracks in $0.2 < p_T < 3$ GeV/c. The results incorporate the uncertainties arising from track selection, reconstruction efficiency, background events, and correlations unrelated to flow (Methods).

Results. To directly observe the shape-size correlation depicted in Fig. 1e-f, we analyze the 0–0.5% most central collisions, and correlate $\langle v_2^2 \rangle$ with event-wise δp_T values (Fig. 2a). A pronounced anticorrelation in U+U
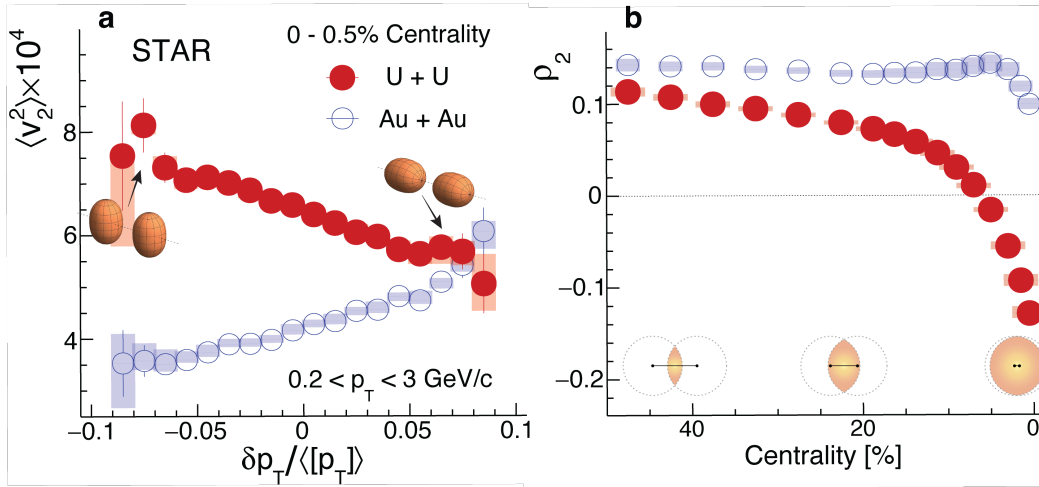
Fig. 2 | Correlation between elliptic flow and radial flow. **a**, $\langle v_2^2 \rangle$ versus $\delta p_{\mathrm{T}}/\langle [p_{\mathrm{T}}]\rangle$ in 0–0.5% most central Au+Au and U+U collisions. **b**, $\rho_2 = \frac{\langle v_2^2 \delta p_{\mathrm{T}}\rangle}{\langle v_2^2 \rangle \sqrt{\langle (\delta p_{\mathrm{T}})^2\rangle}}$ across centrality, quantifying the strength of v_2–δp_{T} correlation. The elliptic-shaped overlaps in the transverse plane for various centralities are also illustrated.

collisions aligns with the expectation [32]: events with small (large) δp_{T} are enriched with body-body (tip-tip) collisions. This effect is striking, as $\langle v_2^2 \rangle$ in U+U is twice that of Au+Au at the lowest δp_{T}, yet similar at the highest δp_{T}.

We quantify this correlation using normalized covariance $\rho_2 = \frac{\langle v_2^2 \delta p_{\mathrm{T}}\rangle}{\langle v_2^2 \rangle \sqrt{\langle (\delta p_{\mathrm{T}})^2\rangle}}$ (Fig. 2b). In Au+Au collisions, ρ_2 stays relatively constant, with a minor decrease in central regions due to centrality smearing [48]. This smearing can be reduced by averaging over a wider, say 0–5% centrality range [49]. In contrast, ρ_2 in U+U collisions decreases steadily, turning negative at about 7% centrality, reflecting the large prolate deformation of ^{238}U. The deformation has the greatest impact in central collisions but also influences other centrality ranges.

Values of observable in one collision system are heavily influenced by QGP properties during hydrodynamic evolution. These final state effects are largely mitigated by taking ratios between the two systems: $R_{\mathcal{O}} = \langle \mathcal{O}\rangle_{\mathrm{U+U}}/\langle \mathcal{O}\rangle_{\mathrm{Au+Au}}$ (Methods). Figure 3a–c show ratios for the three observables. Clearly, $R_{v_2^2}$ and $R_{(\delta p_{\mathrm{T}})^2}$ increase by up to 60% in central collisions, suggesting a large $\beta_{2\mathrm{U}}$, while $R_{v_2^2 \delta p_{\mathrm{T}}}$ decreases by up to threefold across centralities, indicating both a large $\beta_{2\mathrm{U}}$ and a small γ_{U}. The ratios in the 0–5% most central range, having the greatest sensitivity to ^{238}U shape, are visualized as hatch bands in Fig. 3d–f.

The data are compared with the state-of-the-art IP-Glasma+MUSIC hydrodynamic model [26, 50], which combines the fluctuating initial energy density distributions, relativistic viscous hydrodynamics, and hadronic transport. This model, successful in describing various flow observables at both RHIC and the LHC [50], parameterizes nuclear shapes with a deformed Woods-Saxon profile,

$$\rho(r,\theta,\phi) \propto [1 + \exp(r - R(\theta,\phi))/a]^{-1}. \qquad (3)$$

The deformation parameters for Au are fixed to an oblate shape with $\beta_{2\mathrm{Au}} = 0.14$, while those for U are varied. The model also considers final state effects by adjusting QGP viscosities and initial condition uncertainties, including variations in nuclear radius R_0, skin a, $\beta_{2\mathrm{Au}}$, and higher-order shapes (Table 1 in Methods). These variations are included in the model uncertainties. The mass numbers of Au and U, differing by only 20%, result in almost complete cancellation of final state effects, leaving model uncertainties predominantly due to variations in initial conditions. In Fig. 3a-c, calculations for $\beta_{2\mathrm{U}} = 0.28$ match central data for $R_{(\delta p_{\mathrm{T}})^2}$ and $R_{v_2^2 \delta p_{\mathrm{T}}}$, but overestimates $R_{v_2^2}$ in 0–30% centrality. This overestimation could stem from the model's limitations in describing $\varepsilon_2^{\mathrm{rp}}$-related v_2 components, which are more affected by structural parameters like nuclear radius and skin [51]. Thus, the $R_{v_2^2}$ comparison only sets a lower bound for $\beta_{2\mathrm{U}}$.

In Fig. 3d-f, we contrast the 0–5% central data against predictions for varying $\beta_{2\mathrm{U}}$ and γ_{U}. Calculated $R_{v_2^2}$ and $R_{(\delta p_{\mathrm{T}})^2}$ change linearly with $\beta_{2\mathrm{U}}^2$, while $R_{v_2^2 \delta p_{\mathrm{T}}}$ follows a $\beta_{2\mathrm{U}}^3 \cos(3\gamma_{\mathrm{U}})$ trend, aligning remarkably with Eq. (2). The intersections between data and model delineate preferred $\beta_{2\mathrm{U}}$ ranges, yielding $\beta_{2\mathrm{U}}(R_{v_2^2}) = 0.240 \pm 0.014$ and $\beta_{2\mathrm{U}}(R_{(\delta p_{\mathrm{T}})^2}) = 0.294 \pm 0.021$. For $R_{v_2^2 \delta p_{\mathrm{T}}}$, the favored $\beta_{2\mathrm{U}}$ range varies with γ_{U}. These preferred ranges are summarized in Fig. 3g. Since $\beta_{2\mathrm{U}}(R_{v_2^2})$ value is viewed as a lower limit, a combined analysis of constraints from $R_{(\delta p_{\mathrm{T}})^2}$ and $R_{v_2^2 \delta p_{\mathrm{T}}}$ is performed, leading to $\beta_{2\mathrm{U}} = 0.297 \pm 0.013$ and $\gamma_{\mathrm{U}} = 8.6° \pm 4.8°$ (mean and one standard deviation, see Methods).

The extracted $\beta_{2\mathrm{U}}$ value is broadly in line with low-

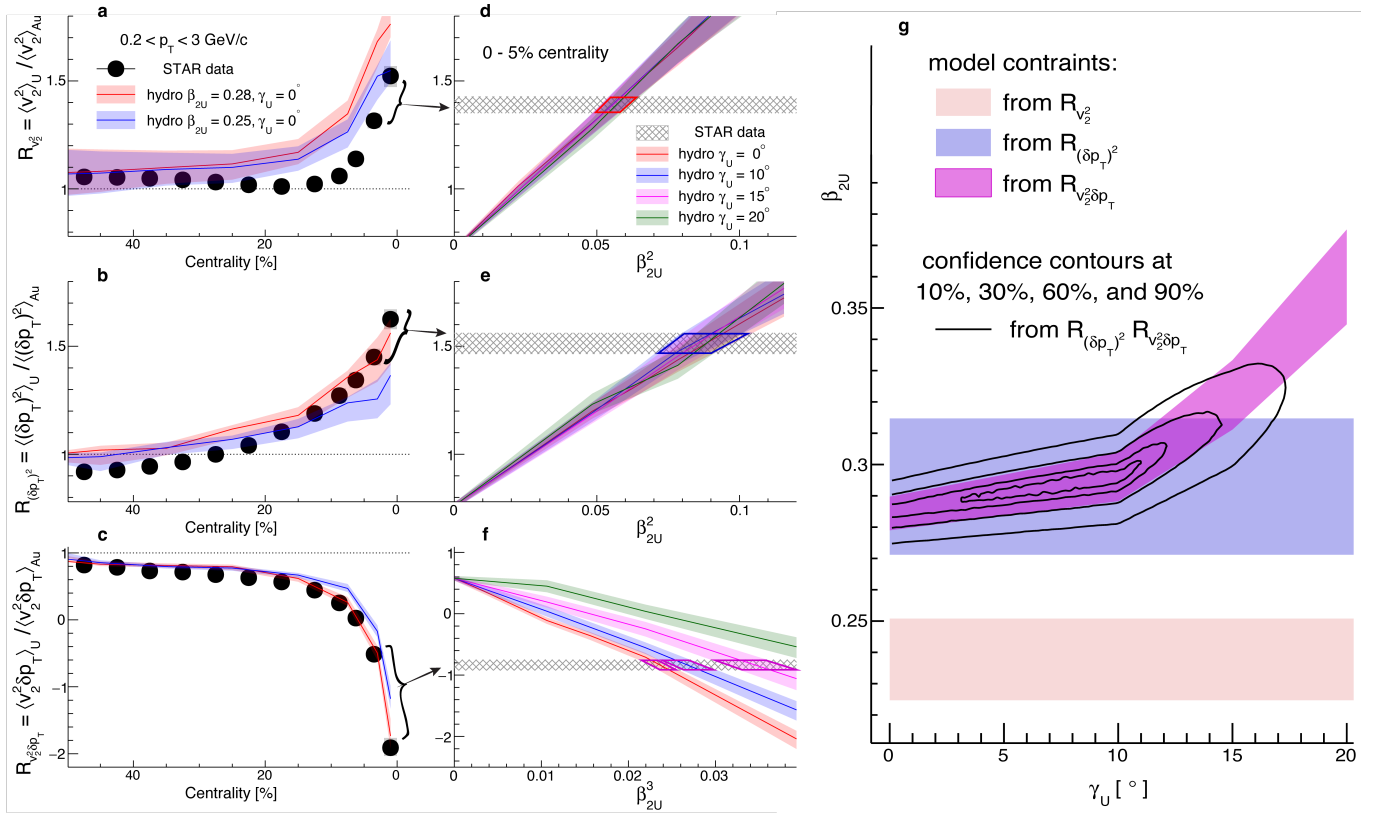**Fig. 3 | Constraining the shape of** ^{238}**U.** Left column: ratios of $\langle v_2^2 \rangle$ (**a**), $\langle (\delta p_{\rm T})^2 \rangle$ (**b**), and $\langle v_2^2 \delta p_{\rm T} \rangle$ (**c**) between U+U and Au+Au collisions as a function of centrality. The data are compared to the IP-Glasma+MUSIC hydrodynamic model calculation assuming $\beta_{2\rm U} = 0.28$ (red) and $\beta_{2\rm U} = 0.25$ (blue), whose shaded bands denote the model uncertainties (Methods). Mid-column: ratio values in 0–5% most central collisions (hatch bands) for $\langle v_2^2 \rangle$ (**d**) and $\langle (\delta p_{\rm T})^2 \rangle$ (**e**), and $\langle v_2^2 \delta p_{\rm T} \rangle$ (**f**) are compared to model calculations as a function of $\beta_{2\rm U}^2$ or $\beta_{2\rm U}^3$ for four $\gamma_{\rm U}$ values. The colored quadrilaterals delineates the allowed ranges of $\beta_{2\rm U}^2$ or $\beta_{2\rm U}^3$ from this data-model comparison. **g** shows the constrained ranges of $(\beta_{2\rm U}, \gamma_{\rm U})$ from three observables separately, and the confidence contours obtained by combining $\langle (\delta p_{\rm T})^2 \rangle$ and $\langle v_2^2 \delta p_{\rm T} \rangle$ (solid lines). The constraint from $R_{v_2^2}$ is viewed as a lower limit and hence is not used (see text).

energy estimates [35–37], implying other sources of nucleon, quark and gluon correlations in ^{238}U are less impactful compared to its large deformation, as supported by recent model studies [24]. Meanwhile, the nonzero $\gamma_{\rm U}$ value, highlighted by the confidence contours in Fig. 3g, suggests a small rigid triaxial component in ^{238}U deformation, consistent with expectations from Ref. [45]. This marks the first indication of nuclear ground state triaxiality without involving transitions to excited states.

Applications. We have demonstrated that flow-assisted imaging is a promising tool for exploring the structure of atomic nuclei in their ground state, complementary to the traditional approaches. The method's strength lies in capturing a fast snapshot of nucleon spatial distribution, applicable to any collision species. This contrasts with nuclear spectroscopy, where complexity and interpretation vary with nucleus's position on the nuclide chart. This approach is effective for discerning shape differences between species with similar mass num-

bers, ideally isobar pairs. Many applications are possible, with a few examples given here:

- Odd-mass nuclides: For odd-mass nuclei, where either N or Z is odd, the nuclear shape is often presumed or determined via laser spectroscopy method [4] to be similar to adjacent even-even nuclei. However, the spectroscopic data are more complex [1] due to the coupling of the single unpaired nucleon with the nuclear core. By comparing the flow observables of odd-mass nuclei to selected even-even neighbors with known shapes, the high-energy approach avoids this complication,

- Octupole and hexadecapole deformations: These less common and generally weaker deformations [52] can be probed through measurement of higher-order flow harmonics (triangular and quadrangular flows).

- Dynamic deformations in "soft" nuclei: This

method could distinguish between average deformation and transient shape fluctuations via measurements of multi-particle correlations [53, 54]. This technique, sensitive only to the ground state, also sidesteps the complexities of disentangling shape variations during transitions to nuclear excited states.

- $0\nu\beta\beta$ decay: The decay rate hinges on nuclear matrix elements (NME), significantly affected by the shapes of the initial and final species – a pair of isobars with the same mass number. Present NME uncertainties, partly stemming from inadequate knowledge of nuclear shapes, pose a major challenge in experimental design [11]. This method, tailored for isobars, allows for the precise determination of shape differences between these species. This could reduce NME uncertainties, and hence aid in experiments searching for $0\nu\beta\beta$ decay and enhance our understanding of neutrino properties.

It would be remiss not to mention that this approach also holds promise in advancing the study of QGP, particularly its dynamics and transport properties, which have been limited by a poor understanding of QGP initial conditions [5, 6] (Fig. 1e). By contrasting flow observables in similarly massed but structurally different species, our technique effectively eliminates final-state effects, thereby isolating initial condition variations seeded by shape differences. This can elucidate mechanisms of initial condition formation, consequently help to improve QGP transport property extraction through Bayesian inferences [55–57], and lead to breakthroughs in high-energy nuclear physics.

Collective flow assisted nuclear shape imaging is a discovery tool for exploring nuclear structure and high-energy nuclear collision physics. Future research could leverage colliders to conduct experiments with selected isobaric or isobar-like pairs. The combination of high- and low-energy techniques enables interdisciplinary opportunities in the study of atomic nuclei across energy scales.

METHODS

Accessing information in the intrinsic frame

The nuclear shape in the intrinsic frame was considered not directly observable in low-energy experiments. In high-energy collisions, the collective flow phenomenon can be used to infer the shape and size of the nucleon distribution in the overlap region of the transverse plane, represented as $\rho(\mathbf{r})$ with $\mathbf{r} = x + iy$, and hence connect directly to the shape characteristics of the two colliding nuclei in their intrinsic frame as discussed below.

The elliptic shape of the heavy-ion initial state is characterized by its amplitude ε_2 and direction Φ_2, which are defined by nucleon positions as,

$$\mathcal{E}_2 \equiv \varepsilon_2 e^{2i\Phi_2} = \frac{\int_{\mathbf{r}} \mathbf{r}^2 \rho(\mathbf{r})}{\int_{\mathbf{r}} |\mathbf{r}|^2 \rho(\mathbf{r})}, \int_{\mathbf{r}} = \int \mathrm{d}x \mathrm{d}y . \qquad (4)$$

It is important to note that when the coordinate system is rotated such that x and y coincide with the minor and major axes, the elliptic eccentricity coincides with the usual definition $\varepsilon_2 = \frac{\langle y^2 \rangle - \langle x^2 \rangle}{\langle y^2 \rangle + \langle x^2 \rangle}$.

The parameter ε_2 plays a crucial role in driving the elliptic flow v_2 of the particle distribution: $v_2 \propto \varepsilon_2$. In general, n-particle correlations quantify the nth-moments of elliptic flow and radial flow distributions, which are linearly related to the nth-moments of ε_2 and $d_\perp$.

To demonstrate this point, let's consider collisions at zero impact parameter without loss of generality, where average elliptic geometry vanishes $\langle \mathcal{E}_2 \rangle = 0$. The second moment of eccentricity for many events becomes [58, 59],

$$\langle \varepsilon_2^2 \rangle = \langle \mathcal{E}_2 \mathcal{E}_2^* \rangle \approx \frac{\int_{\mathbf{r}_1, \mathbf{r}_2} (\mathbf{r}_1)^2 (\mathbf{r}_2^*)^2 \rho(\mathbf{r}_1, \mathbf{r}_2)}{\left(\int_{\mathbf{r}} |\mathbf{r}|^2 \langle \rho(\mathbf{r}) \rangle \right)^2} , \qquad (5)$$

where $\langle \rho(\mathbf{r}) \rangle$ is the event-averaged profile, and

$$\rho(\mathbf{r}_1, \mathbf{r}_2) = \langle \delta\rho(\mathbf{r}_1) \delta\rho(\mathbf{r}_2) \rangle = \langle \rho(\mathbf{r}_1) \rho(\mathbf{r}_2) \rangle - \langle \rho(\mathbf{r}_1) \rangle \langle \rho(\mathbf{r}_2) \rangle$$

is the usual two-body distribution. Similarly, the third central moments are related to the three-body distribution $\rho(\mathbf{r}_1, \mathbf{r}_2, \mathbf{r}_3) = \langle \delta\rho(\mathbf{r}_1) \delta\rho(\mathbf{r}_2) \delta\rho(\mathbf{r}_3) \rangle$. For example,

$$\langle \varepsilon_2^2 \delta d_\perp / d_\perp \rangle \approx -\frac{\int_{\mathbf{r}_1, \mathbf{r}_2, \mathbf{r}_3} (\mathbf{r}_1)^2 (\mathbf{r}_2^*)^2 |\mathbf{r}_3^2| \rho(\mathbf{r}_1, \mathbf{r}_2, \mathbf{r}_3)}{\left(\int_{\mathbf{r}} |\mathbf{r}|^2 \langle \rho(\mathbf{r}) \rangle \right)^2 \int_{\mathbf{r}} |\mathbf{r}|^2 \langle \rho(\mathbf{r}) \rangle} , \quad (6)$$

where we denote $\delta d_\perp / d_\perp \equiv (d_\perp - \langle d_\perp \rangle) / \langle d_\perp \rangle$, and the relation $\frac{\delta d_\perp}{d_\perp} \approx -\frac{\delta \langle |\mathbf{r}^2| \rangle}{\langle |\mathbf{r}^2| \rangle} = -\frac{\int_{\mathbf{r}} |\mathbf{r}^2| \delta\rho(\mathbf{r})}{\int_{\mathbf{r}} |\mathbf{r}^2| \langle \rho(\mathbf{r}) \rangle}$ is used.

The quantities $\mathcal{E}_2$ and $\delta d_\perp / d_\perp$ depend not only on the nuclear shape but also the random orientations of the projectile and target nuclei, denoted by Euler angles Ω_p and Ω_t. For small quadrupole deformation, it suffices to consider the leading-order forms [33]:

$$\frac{\delta d_\perp}{d_\perp} \approx \delta_d + p_0(\Omega_p, \gamma_p)\beta_{2p} + p_0(\Omega_t, \gamma_t)\beta_{2t} ,$$
$$\mathcal{E}_2 \approx \mathcal{E}_0 + \boldsymbol{p}_2(\Omega_p, \gamma_p)\beta_{2p} + \boldsymbol{p}_2(\Omega_t, \gamma_t)\beta_{2t}. \qquad (7)$$

Here the scalar δ_d and vector $\mathcal{E}_0 \equiv \varepsilon_0 e^{2i\Phi_{2;0}}$ represent values for spherical nuclei. The values of scalar p_0 and vector $\boldsymbol{p}_2$ are directly connected to the xy-projected one-body distribution $\rho(\mathbf{r})$. Therefore, they depend on the orientation of the two nuclei. The fluctuations of δ_d ($\mathcal{E}_0$) are uncorrelated with p_0 ($\boldsymbol{p}_2$). After averaging over collisions with different Euler angles and setting $\beta_{2p} = \beta_{2t}$ and $\gamma_p = \gamma_t$, we obtain:

$$\langle \varepsilon_2^2 \rangle = \langle \varepsilon_0^2 \rangle + 2\langle \boldsymbol{p}_2(\gamma) \boldsymbol{p}_2^*(\gamma) \rangle \beta_2^2$$
$$\langle (\delta d_\perp / d_\perp)^2 \rangle = \langle \delta_d^2 \rangle + 2\langle p_0(\gamma)^2 \rangle \beta_2^2$$
$$\langle \varepsilon_2^2 \delta d_\perp / d_\perp \rangle = \langle \varepsilon_0^2 \delta_d \rangle + 2\langle p_0(\gamma) \boldsymbol{p}_2(\gamma) \boldsymbol{p}_2(\gamma)^* \rangle \beta_2^3 . \qquad (8)$$

It is found that $\langle \boldsymbol{p}_2(\gamma)\boldsymbol{p}_2^*(\gamma)\rangle$ and $\langle p_0(\gamma)^2\rangle$ are independent of γ, while $\langle p_0(\gamma)\boldsymbol{p}_2(\gamma)\boldsymbol{p}_2(\gamma)^*\rangle \propto -\cos(3\gamma)$, resulting in expressions in Eq. (2).

The event-averaged moments in Eq. (8) are rotationally invariant and capture the intrinsic many-body distributions of $\rho(\mathbf{r})$. Note that the coefficients a_n in Eq. (2) are strong functions of centrality that decrease towards central collisions, while coefficients b_n change weakly with centrality. Therefore, the impact of deformation is always largest in the most central collisions. In general, it can be shown that the n-particle correlations reflect the rotational invariant n^{th} central moments of $\rho(\mathbf{r})$, which in turn are connected to the nth moments of the nuclear shape in the intrinsic frame.

Previous experimental attempts on nuclear shapes at high energy

The idea that v_2 can be enhanced by β_2 was recognized early [60–64]. Studies at RHIC [65] and the LHC [66–68] in ^{238}U+^{238}U and ^{129}Xe+^{129}Xe collisions indicated β_2's influence on v_2. Several theoretical investigations followed this up to assess the extent to which β_2 can be constrained by v_2 alone [38, 69–71]. A challenge with v_2 is that its a_2 term in Eq. (2) is impacted by $\varepsilon_2^{\mathrm{rp}}$ and often exceeds the $b_1\beta_2^2$ even in central collisions. A recent measurement of $\langle v_2^2 \delta p_{\mathrm{T}}\rangle$ aimed to assess the triaxiality of ^{129}Xe [48], but the extraction of γ_{Xe} was hindered by needing prior knowledge of $\beta_{2\mathrm{Xe}}$ and potentially significant fluctuations in γ_{Xe} [53, 72–74]. The combination of multiple observables allows for more quantitative extraction of nuclear shape parameters, aided by Eq. (2).

Event selection

In high-energy experiments, the polar angle θ is usually mapped to the so-called pseudorapidity variable $\eta = -\ln(\tan(\theta/2))$. The STAR TPC polar angle range $|\theta - 90°| < 50°$ corresponds to $|\eta| < 1$.

The collision events are selected by requiring a coincidence of signals from two vertex position detectors situated on each side of the STAR barrel, covering a pseudorapidity range of $4.4 < |\eta| < 4.9$. To increase the statistics for ultra-central collision (UCC) events, a special sample of Au+Au data in 2010 and U+U data is chosen based on the criteria of high multiplicity in the STAR TPC and minimal activity in the zero-degree calorimeters that cover the beam rapidity [75].

During the offline analysis, events are selected to have collision vertices z_{vtx} within 30 cm of the TPC center along the beam line, and within 2 cm of the beam spot in the transverse plane. Additionally, a selection criterion based on the correlation between the number of TPC tracks and the number of tracks matched to the time-of-flight detector covering $|\eta| < 0.9$ is applied to suppress pileup events (events containing more than one collision in the TPC) [76] and background events.

After applying these selection criteria, the Au+Au data set consists of approximately 528 million minimum-bias events (including 370 million from 2011) and 120 million UCC events. The U+U data set comprises around 300 million minimum-bias events and 5 million UCC events.

Track selection

The charged particle tracks are reconstructed within $|\eta| < 1$ using the TPC [46]. For this analysis, tracks are selected with $|\eta| < 1$ and the transverse momentum range $0.2 < p_{\mathrm{T}} < 3.0$ GeV/c. To ensure good quality, the selected tracks are required to have at least 16 fit points out of a maximum of 45, and the ratio of the number of fit points to the number of possible points must be greater than 0.52. Additionally, to reduce contributions from secondary decays, the distance of the track's closest approach (DCA) to the primary collision vertex is required to be less than 3 cm.

The tracking efficiency in the TPC was evaluated using the standard STAR Monte Carlo embedding technique [77]. The efficiencies are nearly independent of p_{T} for $p_{\mathrm{T}} > 0.5$ GeV/c, with plateau values ranging from 0.72 (0.69) in the most central Au+Au (U+U) collisions to 0.92 in the most peripheral collisions. The efficiency exhibits some p_{T}-dependent variation, on the order of 10% of the plateau values, within the range of $0.2 < p_{\mathrm{T}} < 0.5$ GeV/c.

Centrality

The centrality of each collision is determined using $N_{\mathrm{ch}}^{\mathrm{rec}}$, which represents the number of raw reconstructed tracks in $|\eta| < 0.5$, satisfying $p_{\mathrm{T}} > 0.15$ GeV/c, and having more than 10 fit points. After applying a correction to account for the dependence on the collision vertex position and the luminosity, the distribution of $N_{\mathrm{ch}}^{\mathrm{rec}}$ is compared to a Monte Carlo Glauber calculation [77]. This comparison allows for the determination of centrality intervals expressed as a percentage of the total nucleus-nucleus inelastic cross-section.

Calculation of observables

The $\langle v_2^2 \rangle$, $\langle (\delta p_T)^2 \rangle$, and $\langle v_2^2 \delta p_T \rangle$ are calculated using charged tracks as follows:

$$[p_T] = \frac{\sum_i w_i p_{T,i}}{\sum_i w_i}, \langle\!\langle p_T \rangle\!\rangle \equiv \langle [p_T] \rangle_{\text{evt}}$$

$$\langle (\delta p_T)^2 \rangle = \left\langle \frac{\sum_{i \neq j} w_i w_j (p_{T,i} - \langle\!\langle p_T \rangle\!\rangle)(p_{T,j} - \langle\!\langle p_T \rangle\!\rangle)}{\sum_{i \neq j} w_i w_j} \right\rangle_{\text{evt}}$$

$$\langle v_2^2 \rangle = \left\langle \frac{\sum_{i \neq j} w_i w_j \cos 2(\phi_i - \phi_j)}{\sum_{i \neq j} w_i w_j} \right\rangle_{\text{evt}}$$

$$\langle v_2^2 \delta p_T \rangle = \left\langle \frac{\sum_{i \neq j \neq k} w_i w_j w_k e^{i2\phi_i} e^{-i2\phi_j} (p_{T,k} - \langle\!\langle p_T \rangle\!\rangle)}{\sum_{i \neq j \neq k} w_i w_j w_k} \right\rangle_{\text{evt}}. \quad (9)$$

The averages are performed first on all multiplets within a single event and then over all events in a fixed $N_{\text{ch}}^{\text{rec}}$ bin. The track-wise weights $w_{i,j,k}$ account for tracking efficiency and its η and ϕ-dependent variation. The values of $\langle v_2^2 \rangle$ and $\langle (\delta p_T)^2 \rangle$ are obtained using the standard method, where particle i and j are selected from the $|\eta| < 1$, as well as the two-subevent method, where particle i and j are selected from pseudorapidity ranges of $-1 < \eta_i < -0.1$ and $0.1 < \eta_j < 1$, respectively.

The covariance $\langle v_2^2 \delta p_T \rangle$ is calculated by averaging over all triplets labeled by particle indices i, j, and k. The standard cumulant framework is used to obtain the results instead of directly calculating all triplets [47]. We also calculated $\langle v_2^2 \delta p_T \rangle$ using the two- and three-subevent methods [48]. In the two-subevent method, particles i and j are taken from ranges of $-1 < \eta_i < -0.1$ and $0.1 < \eta_j < 1$, while particle k can be taken from either subevents. In the three-subevent method, all three particles i, j and k are taken from distinct η ranges, namely $-1 < \eta_i < -0.4$, $0.4 < \eta_j < 1$, and $|\eta_k| < 0.3$. The inclusion of a pseudorapidity gap between the particle pairs or triplets suppresses the short-range "non-flow" correlations arising from resonance decays and jets [78].

The calculation of $\rho_2 = \frac{\langle v_2^2 \delta p_T \rangle}{\langle v_2^2 \rangle \sqrt{\langle (\delta p_T)^2 \rangle}}$ relies on the input values of $\langle v_2^2 \rangle$, $\langle (\delta p_T)^2 \rangle$ and $\langle v_2^2 \delta p_T \rangle$. These components and ρ_2 are shown in Fig. 4 as a function of centrality. In the central region, enhancements of $\langle v_2^2 \rangle$ and $\langle (\delta p_T)^2 \rangle$ are observed in U+U collisions relative to Au+Au collisions, which is consistent with the influence of large β_{2U}. In contrast, the values of $\langle v_2^2 \delta p_T \rangle$ are significantly suppressed in U+U compared to Au+Au collisions across the entire centrality range shown. This suppression is consistent with the negative contribution expected for strong prolate deformation of U as described in Eq. (2).

Influence of non-flow correlations

The results in Fig. 4 are obtained using the two-subevent method. However, as discussed earlier, $\langle v_2^2 \delta p_T \rangle$ has contributions from non-flow correlations, which can be explored by comparing results obtained from the standard, two-subevent and three-subevent methods. The results for ρ_2 are shown in Fig. 5. In this figure, $\langle v_2^2 \rangle$ and $\langle (\delta p_T)^2 \rangle$ are calculated using the two-subevent method, so any variations in ρ_2 arise only from $\langle v_2^2 \delta p_T \rangle$.

Differences are observed between the standard and subevent methods, particularly in peripheral collisions. The majority of the variations arise from the comparison between the standard and two-subevent methods, while the differences between the two- and three-subevent methods are relatively small. It is worth mentioning that some of these differences can be attributed to longitudinal fluctuations in $[p_T]$ and v_2 [48, 79, 80].

Systematic uncertainties

Systematic uncertainties are estimated by varying the track quality selections, the z_{vtx} cuts, examining the influence of pileup, comparing results from periods with different detector conditions, the possible impact of non-flow contributions, and closure test. The influence of track selection criteria is studied by varying the number of fit hits on the track from a minimum of 16 to 19 and by varying DCA cut from < 3 cm to < 2.5 cm, resulting in variations of 1–5% for $\langle (\delta p_T)^2 \rangle$. The impacts on $\langle v_2^2 \rangle$ and $\langle v_2^2 \delta p_T \rangle$ are up to 2.5% and 4%, respectively.

The influence of track reconstruction on the collision vertex is examined by comparing the results for different $|z_{\text{vtx}}|$ cuts, with differences found to be 0.5–3% for all observables. Comparisons between different data-taking periods, particularly normal and reverse magnetic field runs in Au+Au collisions, show consistency within their statistical uncertainties. The influence of pileup and background events is studied by varying the cut on the correlation between $N_{\text{ch}}^{\text{rec}}$ and the number of hits in the TOF. The influence is found to be 1–3% for $\langle v_2^2 \rangle$ and $\langle (\delta p_T)^2 \rangle$, and reaches 2–10% for $\langle v_2^2 \delta p_T \rangle$. Comparisons are also made between the 2010 and 2011 Au+Au datasets, which have different active acceptances in the TPC. The results are largely consistent with the quoted uncertainties, although some differences are observed, particularly in the central region, where variations reach 5–10% for $\langle v_2^2 \delta p_T \rangle$.

A closure test was conducted, wherein the reconstruction efficiency and its variations in η and ϕ from the data were utilized to retain a fraction of the particles generated from a multi-phase transport model [81]. Subsequently, a track-by-track weight, as described in Eq. 9, was applied to the accepted particles. All observables are calculated using the accepted particles and compared to those obtained using the original particles. This procedure allowed us to recover $\langle v_2^2 \rangle$ and $\langle (\delta p_T)^2 \rangle$ within their statistical uncertainties. However, a 2–3% nonclo-

sure was observed in $\langle v_2^2 \delta p_T \rangle$. Nevertheless, it's important to note that such non-closures largely cancel out when considering the ratios between U+U and Au+Au collisions.

Several additional cross-checks were also carried out. The track reconstruction efficiency has an approximate 5% uncertainty due to its reliance on particle type and occupancy dependence. We repeated the analysis by varying this efficiency, and the variations in the results were either less than 1% or consistent with their statistical uncertainties. The reconstructed p_T can differ from the true value due to finite momentum resolution. This effect was investigated by further smearing the reconstructed p_T according to the known resolution, calculating the observable, and comparing the results with the original ones. A discrepancy of approximately 0.5% was observed for $\langle (\delta p_T)^2 \rangle$, while other observables remained consistent within their statistical uncertainties. These effects cancel in the ratios between U+U and Au+Au collisions.

Modest differences are observed between the standard method and subvent methods for all observables, particularly towards the peripheral collisions. Some of these differences are attributable to non-flow contributions, while the remainder could arise from longitudinal flow decorrelations. We obtain default results as the average of the standard method and two-subevent method, and half of the differences are assigned as systematic uncertainties. They are 1–2% for $\langle v_2^2 \rangle$, 1–3% for $\langle (\delta p_T)^2 \rangle$, and 2–4% for $\langle v_2^2 \delta p_T \rangle$ in the 0–40% centrality range, respectively.

The total systematic uncertainties are combined in quadrature from different sources, and in some cases, they are larger than the statistical uncertainties. The total uncertainties of $\langle v_2^2 \rangle$, $\langle (\delta p_T)^2 \rangle$, and $\langle v_2^2 \delta p_T \rangle$ are 2.5–4%, 2–5%, and 4–10%, respectively. Note that for the ratios between U+U and Au+Au, their uncertainties are evaluated for each source and combined in quadrature to form the total systematic uncertainties. This process results in a partial cancellation of the uncertainties between the two systems.

Assigning uncertainties on β_{2U} and γ_U

A standard pseudo-experiment procedure, similar to that described in Ref. [82], is employed to combine the uncertainties from $R_{(\delta p_T)^2}$ and $R_{v_2^2 \delta p_T}$ shown in Fig. 3g. We assume that the total uncertainties extracted from the two observables are independent, and we model the probability density function as follows:

$$P(\beta_{2U}, \gamma_U) \propto \exp\left(-\frac{(\beta_{2U} - \bar{\beta}_a)^2}{2\sigma_a^2} - \frac{(\beta_{2U} - \bar{\beta}_b(\gamma_U))^2}{2\sigma_b^2(\gamma_U)} \right). \tag{10}$$

Here, $\bar{\beta}_a = 0.294$ and $\sigma_a = 0.021$ represent the mean and uncertainty of β_{2U} extracted from $R_{(\delta p_T)^2}$ in Fig. 3g.

Similarly, $\bar{\beta}_b$ and σ_b are the mean and uncertainty of β_{2U} from $R_{v_2^2 \delta p_T}$, and they depend on the parameter γ_U. We sample a uniform prior distribution in β_{2U} and γ_U to obtain the posterior distribution. From this posterior distribution, we obtained the mean and one standard deviation uncertainty of β_{2U} and γ_U, as well as the confidence contours displayed in Fig. 3g.

We also performed an extraction using all three ratio observables. In this case, an additional Gaussian probability density function derived for $R_{v_2^2}$ with a mean $\bar{\beta}_c = 0.240$ and variance $\sigma_c = 0.014$ is multiplied to Eq. (10), and the same procedure described above is repeated. This gives $\beta_{2U} = 0.281 \pm 0.010$ and $\gamma_U = 4.4° \pm 3.2°$. However, we do not use this estimate, given the imperfect description of v_2 in the hydrodynamic model.

Hydrodynamic model setup and simulation

Table 1 details the Woods-Saxon parameters for Au and U used in the IP-Glasma+MUSIC model calculations. The nucleon-nucleon inelastic cross-sections are chosen to be the standard values 42 mb and 40.6 mb for Au+Au collisions at 200 GeV and U+U collisions at 193 GeV, respectively. For U, the nuclear shape in Eq. (1) is extended to include a possible small axial hexadecapole deformation β_4:

$$R(\theta, \phi) = R_0(1 + \beta_2[\cos\gamma Y_{2,0} + \sin\gamma Y_{2,2}] + \beta_4 Y_{4,0}). \tag{11}$$

Most low-energy nuclear structure models favor a modest oblate deformation for ^{197}Au [34] in the range of $\beta_{2Au} \approx 0.12 - 0.14$. We assume ^{197}Au is oblate shape with $\beta_{2Au} = 0.14$ as the default choice for simulation. For ^{238}U, we have scanned several β_{2U} values ranging from 0 to 0.34. We also vary β_{4U} from 0 to 0.09 and γ_U in the range of $0°$–$20°$ to examine the sensitivity of the U+U results to hexadecapole deformation and triaxiality. For each setting, about 100,000–400,000 events are generated using the officially available IP-Glasma+MUSIC [26, 50]. Each event is oversampled at least 100 times to minimize non-flow effects and statistical fluctuations in the hadronic transport. These calculations were performed using services provided by the Open Science Grid (OSG) Consortium [83, 84].

The role of final state effects is studied by varying the shear and bulk viscosities simultaneously up and down by 50%. The impact on $\langle v_2^2 \rangle$ and $\langle (\delta p_T)^2 \rangle$ and $\langle v_2^2 \delta p_T \rangle$ are shown for Au+Au collisions in top of panels of Fig. 6. The values of these flow observables are changed by more than a factor of two as a function of centrality, yet the ratios between U+U and Au+Au collisions, shown in the bottom panels, are relatively stable. A small reduction of $R_{v_2^2}$ and $R_{(\delta p_T)^2}$ are observed in the non-central collisions, when values of viscosities are halved. However, this change is clearly an overestimate since the calculated flow observables greatly overestimate the data. So in the

end, half of the variations of the ratios are included in the model uncertainty.

The main theoretical uncertainties arise from variations in nuclear structure parameters. Parameters common between two collision systems, such as the minimum inter-nucleon distance in nuclei $d_{\min}$, are not expected to contribute to the uncertainty significantly. However, other parameters including nuclear radius R_0, skin a, and higher-order deformation β_4 could be different between Au and U, and hence contribute more to the theoretical uncertainty.

Table 1 provides a list of variations of nuclear structure parameters. The impact of these variations on ratios of flow observables is displayed in Fig. 7. The ratios of flow observables are insensitive to these variations in the most central collisions. Clearly, $R_{v_2^2}$ is particularly sensitive to skin parameter a. This is understandable, as v_2 has a large contribution from the reaction plane flow, which varies strongly with the value of a [51].

Model uncertainties for the ratios are derived by combining the impact of varying viscosities, together with various sources from Fig. 7 according to the Barlow prescription [85]. As a consequence, checks that are consistent with the default calculation within their statistical uncertainties do not contribute to the model uncertainties. The combined model uncertainties for one standard deviation are illustrated in Fig. 3.

A cross-check was also carried out for an alternative hydrodynamic code, the Trajectum model [86, 87]. This model has 20 parameter sets obtained from a Bayesian analysis of the Pb+Pb data at the LHC, but was unfortunately not tuned to the RHIC data. For this calculation, we simply repeat the calculation at RHIC energy and calculate the same observables. While the description of the $\langle v_2^2 \rangle$ and $\langle (\delta p_T)^2 \rangle$ is reasonable, several parameter sets give negative values of $\langle v_2^2 \delta p_T \rangle$ in mid-central collisions, and subsequently not used. The calculation is performed for the remaining 16 parameter sets as a function of centrality, and root mean square variation among these calculations is assigned as the uncertainty.

Figure 8 displays the ratios of flow observables from Trajectum and compares them to IP-Glasma+MUSIC. The results from these two models agree within their uncertainties for $R_{v_2^2}$ and $R_{(\delta p_T)^2}$, with Trajectum predictions slightly higher in the UCC region. This leads to slightly lower values of β_{2U}: $\beta_{2U} = 0.230 \pm 0.010$ for $R_{v_2^2}$ and $\beta_{2U} = 0.273 \pm 0.015$ for $R_{(\delta p_T)^2}$.

For $R_{v_2^2 \delta p_T}$, however, the Trajectum model tends to under-predict the data. In central collisions, such discrepancy can be improved by adjusting the triaxiality parameter to $\gamma_U = 15°$. Overall, the comparison of the Trajectum model with data leads to similar constraints on β_{2U} but slightly larger γ_U.

Table 1 | The choices of Woods-Saxon parameters in Eqs. (3) and (11), including deformations, in the IP-Glasma+MUSIC model. The default values are denoted by bold font, while the rest are variations designed to constrain the values of (β_{2U}, γ_U) and derive theoretical uncertainties associated with other structure parameters.

Species	R(fm)	a (fm)	$d_{\min}$(fm)	β_2	β_4	γ (°)
^{197}Au	**6.62**,6.38	**0.52**	**0.9**, 0.4	**0.14**,0.12	**0**	**60**
^{238}U	**6.81**,7.07	**0.55** 0.495,0.605	**0.9**, 0.4	0,0.15,0.22 0.25,**0.28**,0.34	**0.09**,0	**0**, 10, 15 20

[1] A. Bohr and B. R. Mottelson, "Nuclear Structure, Vols.I&II," (1998).
[2] K. Heyde and J. L. Wood, Phys. Scripta 91, 083008 (2016).
[3] D. Cline, Ann. Rev. Nucl. Part. Sci. 36, 683 (1986).
[4] X. F. Yang, S. J. Wang, S. G. Wilkins, and R. F. Garcia Ruiz, Prog. Part. Nucl. Phys. 129, 104005 (2023), arXiv:2209.15228 [nucl-ex].
[5] E. Shuryak, Rev. Mod. Phys. 89, 035001 (2017), arXiv:1412.8393 [hep-ph].
[6] W. Busza, K. Rajagopal, and W. van der Schee, Ann. Rev. Nucl. Part. Sci. 68, 339 (2018), arXiv:1802.04801 [hep-ph].
[7] R. Hofstadter, Rev. Mod. Phys. 28, 214 (1956).
[8] P. Möller, A. J. Sierk, T. Ichikawa, and H. Sagawa, Atom. Data Nucl. Data Tabl. 109-110, 1 (2016), arXiv:1508.06294 [nucl-th].
[9] H. Schatz et al., Phys. Rept. 294, 167 (1998).
[10] N. Schunck and D. Regnier, Prog. Part. Nucl. Phys. 125, 103963 (2022), arXiv:2201.02719 [nucl-th].
[11] J. Engel and J. Menéndez, Rept. Prog. Phys. 80, 046301 (2017), arXiv:1610.06548 [nucl-th].
[12] Y. Toh et al., Phys. Rev. C 87, 041304 (2013).
[13] T. Nakatsukasa, K. Matsuyanagi, M. Matsuo, and K. Yabana, Rev. Mod. Phys. 88, 045004 (2016), arXiv:1606.04717 [nucl-th].
[14] K. Heyde and J. L. Wood, Rev. Mod. Phys. 83, 1467 (2011).
[15] M. Bender, P.-H. Heenen, and P.-G. Reinhard, Rev. Mod. Phys. 75, 121 (2003).
[16] M. Riordan and W. Zajc, Scientific American 294, 34 (2006).
[17] C. Gale, S. Jeon, and B. Schenke, Int. J. Mod. Phys. A 28, 1340011 (2013), arXiv:1301.5893 [nucl-th].
[18] Z. Vager, R. Naaman, and E. P. Kanter, Science 244, 426 (1989).
[19] M. Kunitski et al., Science 348, 551 (2015), arXiv:1512.02036 [physics.atm-clus].
[20] T. Endo et al., Science 370, 1072 (2020).
[21] R. Boll, J. M. Schäfer, B. Richard, K. Fehre, G. Kastirke, Z. Jurek, and et al., Nature Physics 18, 423 (2022).
[22] J. L. Miller, Physics Today 75, 12 (2022), https://pubs.aip.org/physicstoday/article-pdf/75/5/12/16424077/12_1_online.pdf.

[23] W. Nazarewicz, *Nuclear Structure at the Limits, Proceedings of the Eleventh Physics Summer School Frontiers in Nuclear Physics* (World Scientific, Singapore, 1998).

[24] H. Mäntysaari, B. Schenke, C. Shen, and W. Zhao, Phys. Rev. Lett. **131**, 062301 (2023), arXiv:2303.04866 [nucl-th].

[25] J.-Y. Ollitrault, Phys. Rev. D **46**, 229 (1992).

[26] B. Schenke, C. Shen, and D. Teaney, Phys. Rev. C **102**, 034905 (2020), arXiv:2004.00690 [nucl-th].

[27] J. Adams *et al.* (STAR), Nucl. Phys. A **757**, 102 (2005), arXiv:nucl-ex/0501009.

[28] K. Adcox *et al.* (PHENIX), Nucl. Phys. A **757**, 184 (2005), arXiv:nucl-ex/0410003.

[29] H. Niemi, G. S. Denicol, H. Holopainen, and P. Huovinen, Phys. Rev. C **87**, 054901 (2013), arXiv:1212.1008 [nucl-th].

[30] P. Bożek and W. Broniowski, Phys. Rev. C **85**, 044910 (2012), arXiv:1203.1810 [nucl-th].

[31] B. Alver *et al.* (PHOBOS), Phys. Rev. C **77**, 014906 (2008), arXiv:0711.3724 [nucl-ex].

[32] G. Giacalone, Phys. Rev. Lett. **124**, 202301 (2020), arXiv:1910.04673 [nucl-th].

[33] J. Jia, Phys. Rev. C **105**, 044905 (2022), arXiv:2109.00604 [nucl-th].

[34] B. Bally, G. Giacalone, and M. Bender, Eur. Phys. J. A **59**, 58 (2023), arXiv:2301.02420 [nucl-th].

[35] S. Raman, C. Malarkey, W. Milner, C. Nestor, and P. Stelson, Atomic Data and Nuclear Data Tables **36**, 1 (1987).

[36] J. P. Delaroche, M. Girod, J. Libert, H. Goutte, S. Hilaire, S. Péru, N. Pillet, and G. F. Bertsch, Phys. Rev. C **81**, 014303 (2010).

[37] B. Pritychenko, M. Birch, B. Singh, and M. Horoi, Atom. Data Nucl. Data Tabl. **107**, 1 (2016), [Erratum: Atom.Data Nucl.Data Tabl. 114, 371–374 (2017)], arXiv:1312.5975 [nucl-th].

[38] W. Ryssens, G. Giacalone, B. Schenke, and C. Shen, Phys. Rev. Lett. **130**, 212302 (2023), arXiv:2302.13617 [nucl-th].

[39] K. LÖBNER, M. VETTER, and V. HÖNIG, Atomic Data and Nuclear Data Tables **7**, 495 (1970).

[40] A. Hayashi, K. Hara, and P. Ring, Phys. Rev. Lett. **53**, 337 (1984).

[41] J. A. Sheikh and K. Hara, Phys. Rev. Lett. **82**, 3968 (1999), arXiv:nucl-th/9812051.

[42] C. Y. Wu and D. Cline, Phys. Rev. C **54**, 2356 (1996).

[43] S. P. Rouoof, N. Nazir, S. Jehangir, G. H. Bhat, J. A. Sheikh, N. Rather, and S. Frauendorf, (2023), arXiv:2307.06670 [nucl-th].

[44] J. F. Sharpey-Schafer, R. A. Bark, S. P. Bvumbi, T. R. S. Dinoko, and S. N. T. Majola, Eur. Phys. J. A **55**, 15 (2019).

[45] T. Otsuka, Y. Tsunoda, Y. Utsuno, N. Shimizu, T. Abe, and H. Ueno, (2023), arXiv:2303.11299 [nucl-th].

[46] M. Anderson *et al.*, Nucl. Instrum. Meth. A **499**, 659 (2003), arXiv:nucl-ex/0301015.

[47] A. Bilandzic, R. Snellings, and S. Voloshin, Phys. Rev. C **83**, 044913 (2011), arXiv:1010.0233 [nucl-ex].

[48] G. Aad *et al.* (ATLAS), Phys. Rev. C **107**, 054910 (2023), arXiv:2205.00039 [nucl-ex].

[49] M. Zhou and J. Jia, Phys. Rev. C **98**, 044903 (2018), arXiv:1803.01812 [nucl-th].

[50] B. Schenke, C. Shen, and P. Tribedy, Phys. Rev. C **102**, 044905 (2020), arXiv:2005.14682 [nucl-th].

[51] J. Jia, G. Giacalone, and C. Zhang, Phys. Rev. Lett. **131**, 022301 (2023), arXiv:2206.10449 [nucl-th].

[52] P. A. Butler and W. Nazarewicz, Rev. Mod. Phys. **68**, 349 (1996).

[53] A. Dimri, S. Bhatta, and J. Jia, Eur. Phys. J. A **59**, 45 (2023), arXiv:2301.03556 [nucl-th].

[54] S. Acharya *et al.* (ALICE), Phys. Lett. B **818**, 136354 (2021), arXiv:2102.12180 [nucl-ex].

[55] J. E. Bernhard, J. S. Moreland, and S. A. Bass, Nature Phys. **15**, 1113 (2019).

[56] D. Everett *et al.* (JETSCAPE), Phys. Rev. Lett. **126**, 242301 (2021), arXiv:2010.03928 [hep-ph].

[57] G. Nijs, W. van der Schee, U. Gürsoy, and R. Snellings, Phys. Rev. Lett. **126**, 202301 (2021), arXiv:2010.15130 [nucl-th].

[58] G. Giacalone, P. Guerrero-Rodríguez, M. Luzum, C. Marquet, and J.-Y. Ollitrault, Phys. Rev. C **100**, 024905 (2019), arXiv:1902.07168 [nucl-th].

[59] G. Giacalone, Eur. Phys. J. A **59**, 297 (2023), arXiv:2305.19843 [nucl-th].

[60] B.-A. Li, Phys. Rev. C **61**, 021903 (2000), arXiv:nucl-th/9910030.

[61] E. V. Shuryak, Phys. Rev. C **61**, 034905 (2000), arXiv:nucl-th/9906062.

[62] P. Filip, R. Lednicky, H. Masui, and N. Xu, Phys. Rev. C **80**, 054903 (2009).

[63] Q. Y. Shou, Y. G. Ma, P. Sorensen, A. H. Tang, F. Videbæk, and H. Wang, Phys. Lett. B **749**, 215 (2015), arXiv:1409.8375 [nucl-th].

[64] A. Goldschmidt, Z. Qiu, C. Shen, and U. Heinz, Phys. Rev. C **92**, 044903 (2015), arXiv:1507.03910 [nucl-th].

[65] L. Adamczyk *et al.* (STAR), Phys. Rev. Lett. **115**, 222301 (2015), arXiv:1505.07812 [nucl-ex].

[66] ALICE Collaboration, Phys. Lett. B **784**, 82 (2018), arXiv:1805.01832 [nucl-ex].

[67] A. M. Sirunyan *et al.* (CMS), Phys. Rev. C **100**, 044902 (2019), arXiv:1901.07997 [hep-ex].

[68] G. Aad *et al.* (ATLAS), Phys. Rev. C **101**, 024906 (2020), arXiv:1911.04812 [nucl-ex].

[69] G. Giacalone, J. Noronha-Hostler, M. Luzum, and J.-Y. Ollitrault, Phys. Rev. C **97**, 034904 (2018), arXiv:1711.08499 [nucl-th].

[70] G. Giacalone, Phys. Rev. C **102**, 024901 (2020), arXiv:2004.14463 [nucl-th].

[71] G. Giacalone, J. Jia, and C. Zhang, Phys. Rev. Lett. **127**, 242301 (2021), arXiv:2105.01638 [nucl-th].

[72] L. M. Robledo, R. R. Rodriguez-Guzman, and P. Sarriguren, Phys. Rev. C **78**, 034314 (2008).

[73] B. Bally, M. Bender, G. Giacalone, and V. Somà, Phys. Rev. Lett. **128**, 082301 (2022), arXiv:2108.09578 [nucl-th].

[74] B. Bally, G. Giacalone, and M. Bender, Eur. Phys. J. A **58**, 187 (2022), arXiv:2207.13576 [nucl-th].

[75] F. S. Bieser *et al.*, Nucl. Instrum. Meth. A **499**, 766 (2003).

[76] W. J. Llope (STAR), Nucl. Instrum. Meth. A **661**, S110 (2012).

[77] L. Adamczyk *et al.* (STAR), Phys. Rev. C **92**, 024912 (2015), arXiv:1504.01317 [hep-ex].

[78] J. Jia, M. Zhou, and A. Trzupek, Phys. Rev. C **96**,

034906 (2017), arXiv:1701.03830 [nucl-th].

[79] V. Khachatryan *et al.* (CMS), Phys. Rev. C **92**, 034911 (2015), arXiv:1503.01692 [nucl-ex].

[80] G. Aad *et al.* (ATLAS), Phys. Rev. Lett. **126**, 122301 (2021), arXiv:2001.04201 [nucl-ex].

[81] Z.-W. Lin, C. M. Ko, B.-A. Li, B. Zhang, and S. Pal, Phys. Rev. C **72**, 064901 (2005), arXiv:nucl-th/0411110.

[82] R. Nisius, Eur. Phys. J. C **74**, 3004 (2014), arXiv:1402.4016 [physics.data-an].

[83] R. Pordes, D. Petravick, B. Kramer, D. Olson, M. Livny, A. Roy, P. Avery, K. Blackburn, T. Wenaus, F. Würthwein, I. Foster, R. Gardner, M. Wilde, A. Blatecky, J. McGee, and R. Quick, in *J. Phys. Conf. Ser.*, 78, Vol. 78 (2007) p. 012057.

[84] I. Sfiligoi, D. C. Bradley, B. Holzman, P. Mhashilkar, S. Padhi, and F. Wurthwein, in *2009 WRI World Congress on Computer Science and Information Engineering*, 2, Vol. 2 (2009) pp. 428–432.

[85] R. Barlow, in *Conference on Advanced Statistical Techniques in Particle Physics* (2002) pp. 134–144, arXiv:hep-ex/0207026.

[86] G. Nijs and W. van der Schee, (2023), arXiv:2304.06191 [nucl-th].

[87] G. Giacalone, G. Nijs, and W. van der Schee, Phys. Rev. Lett. **131**, 202302 (2023), arXiv:2305.00015 [nucl-th].
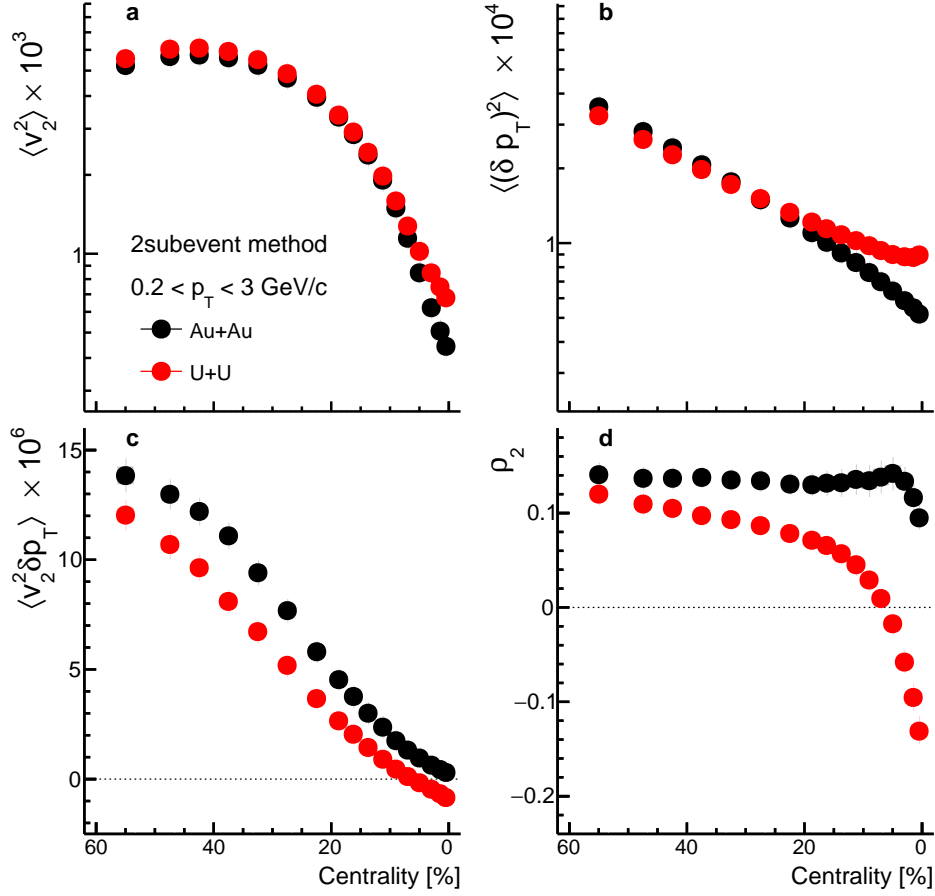
EXTENDED DATA

Fig. 4 | Components involved in v_2-[p_T] correlations. The centrality dependences of $\langle v_2^2 \rangle$ (**a**), $\langle (\delta p_T)^2 \rangle$ (**b**), $\langle v_2^2 \delta p_T \rangle$ (**c**) and $\rho_2 = \frac{\langle v_2^2 \delta p_T \rangle}{\langle v_2^2 \rangle \sqrt{\langle (\delta p_T)^2 \rangle}}$ (**d**) in U+U and Au+Au collisions. They are calculated using the two-subevent method.
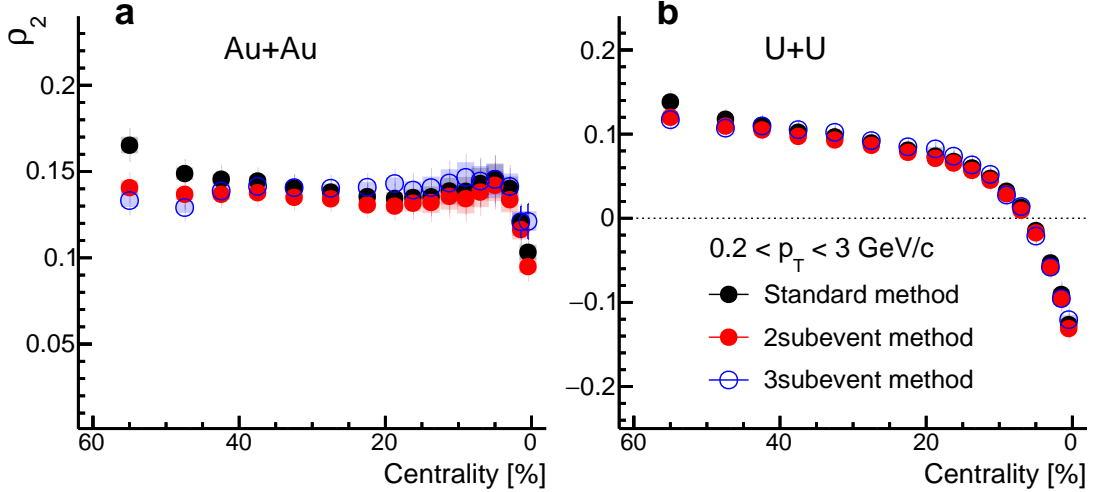

Fig. 5 | Impact of non-flow correlations. The centrality dependence of $\rho_2 = \frac{\langle v_2^2 \delta p_T \rangle}{\langle v_2^2 \rangle \sqrt{\langle (\delta p_T)^2 \rangle}}$ in Au+Au (**a**) and U+U (**b**) collisions, where $\langle v_2^2 \delta p_T \rangle$ is calculated using the standard, two-subevent and three-subevent correlation methods. The components in the denominator $\langle v_2^2 \rangle$ and $\langle (\delta p_T)^2 \rangle$ are calculated using the two-subevent method.
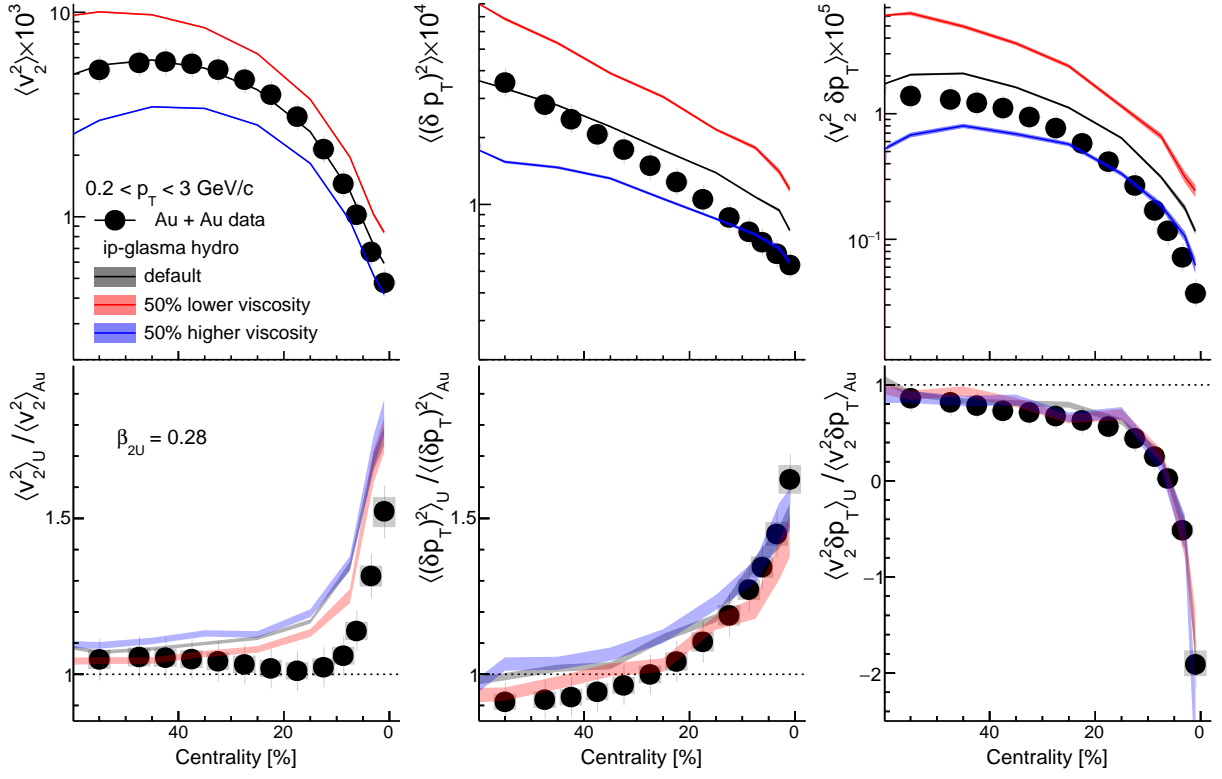
Fig. 6 | Sensitivity to shear and bulk viscosities of the QGP. IP-Glasma+MUSIC model prediction of the $\langle v_2^2 \rangle$ (left), $\langle (\delta p_{\mathrm{T}})^2 \rangle$ (middle) and $\langle v_2^2 \delta p_{\mathrm{T}} \rangle$ (right) compared with the data in Au+Au collisions and the corresponding ratios (bottom) between U+U and Au+Au collisions, for different amount of shear and bulk viscosities.
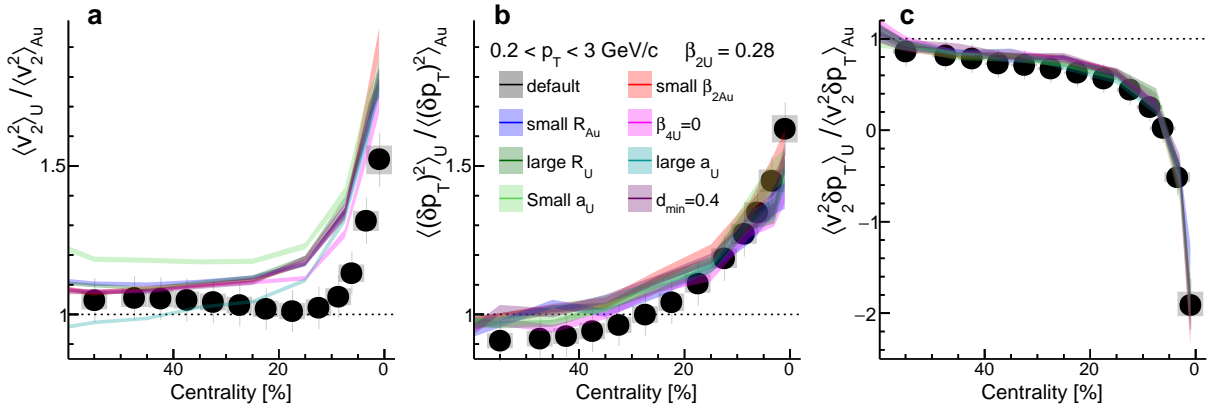

Fig. 7 | Sensitivity to nuclear structure parameters. IP-Glasma+MUSIC model prediction of the ratios of $\langle v_2^2 \rangle$ (**a**), $\langle (\delta p_{\mathrm{T}})^2 \rangle$ (**b**), and $\langle v_2^2 \delta p_{\mathrm{T}} \rangle$ (**c**) between U+U and Au+Au collisions. The calculations are done for different Glauber model parameters and they are compared to the data.
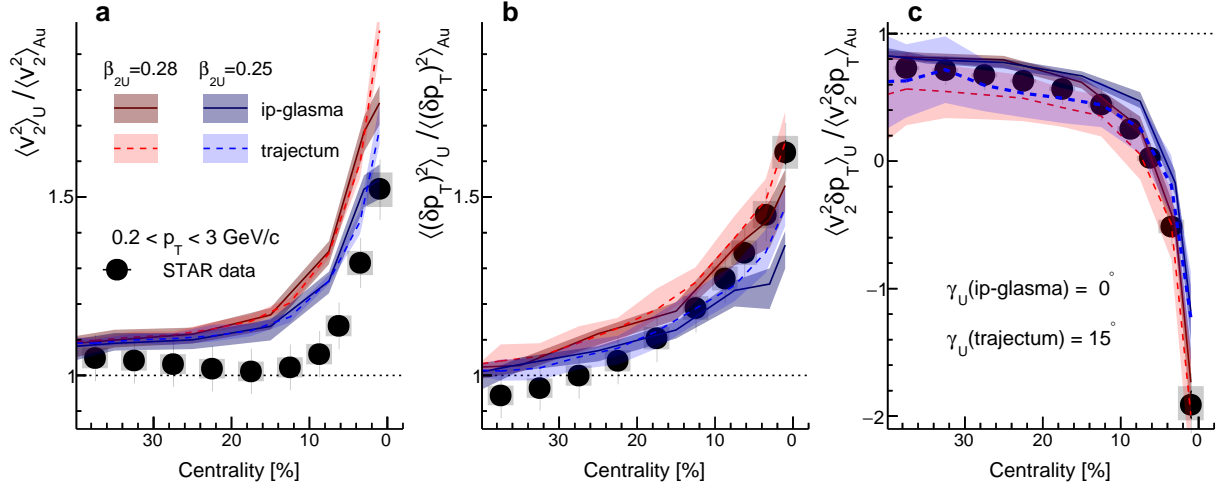
Fig. 8 | Comparison between two hydrodynamic models. The ratios of $\langle v_2^2 \rangle$ (**a**), $\langle (\delta p_T)^2 \rangle$ (**b**) and $\langle v_2^2 \delta p_T \rangle$ (**c**) as a function of centrality from IP-Glasma+MUSIC (solid lines) and Trajectum (dashed lines), assuming $\beta_{2U} = 0.28$ (red) and $\beta_{2U} = 0.25$ (blue). For the IP-Glasma+MUSIC model, only the uncertainties for the default configuration are shown for clarity. They are compared to the data.